Mitosis down-regulates nuclear volume and resets nuclear envelope folding of cancer cells under prolonged confinement

Malèke Mouelhi[1*], Alexis Saffon[1], Hélène Delanoë-Ayari[1], Sylvain Monnier[1+*], Charlotte Rivière[1,2,3+*]

[1] *Univ Lyon, Université Claude Bernard Lyon 1, CNRS, Institut Lumière Matière, UMR 5306, 69622, Villeurbanne, France*
[2] *Institut Universitaire de France (IUF), France*
[3] *Institut Convergence PLAsCAN, Centre de Cancérologie de Lyon, INSERM U1052-CNRS UMR5286, Univ Lyon, Université Claude Bernard Lyon 1, Centre Léon Bérard, Lyon, France*
[+]Senior author contributed equally to this work

[*]Corresponding authors

Abstract

During their life, mammalian cells are subjected to numerous mechanical constraints, especially in pathological contexts such as cancer. Most studies on cell confinement focus on short periods, and little is still known about cell adaptation to prolonged squeezing, over several cell divisions. Using a hydrogel-based confinement system, we reveal the unsuspected role of mitosis in long-term adaptation to prolonged uniaxial confinement, in a contractility-dependent manner. To adapt to the level of confinement and to alleviate the imposed mechanical stress, nuclei are reaching a new homeostatic state following the first confined cell division: cells down-regulate their nuclear volume, together with a reset of their nuclear envelope folding. A simple geometric model suggests that this new nuclear volume is triggered by the apparent surface of the nuclear envelope.

Our findings have important implications for the fundamental understanding of nuclear regulation under mechanical constraints and are critical to better comprehend cancer cells plasticity.

Introduction

Cancer is a leading cause of death worldwide, despite continual progress in therapeutic strategies and in our understanding of cancer cell biology. The role of mechanics in cancer cell response has raised attention over the last decades [1–4], and alleviating mechanical stress is now envisioned as an interesting therapeutic strategy [5,6]. Deformed nuclei within tumors has been reported *in vivo* [7,8], though consequences on cell fate remain unknown. Pioneer works have identified an alteration of cell mitosis

29 under such confined situations [9,10], with modified cell cycle progression and division [11], the presence of
30 multi-daughter events, daughter cells of unequal size, and induction of cell death [12]. Conversely, it has
31 been shown that flattening is required for the G1-S transition [13], as well as the G2-M transition [14]. The
32 role of the nucleus as a mechanosensor is now clearly recognized [15,16], with a mechanism of nuclear
33 repair[17] and rescue of DNA damage [18]. Upon squeezing, the nucleus shortly unfolds its inner lamin
34 envelope, activating the cytosolic phospholipase A2 (cPLA2)-Arachidonic acid (AA) pathway [15], as well as
35 myosin II contractility and switches towards a motile phenotype[16]. Nuclear blebs and chromatin
36 herniation can also occur, leading to transient events of nuclear rupture and repair [17,19]. However, all
37 these studies analyzed the short-term nuclear adaptation (within minutes to a few hours), and cancer
38 cells adaptation to a prolonged imposed deformation (over several days) remains unexplored,
39 specifically how such deformation affects cell cycle progression.
40 We have recently developed an agarose-based soft-confiner, ideal to analyze the proliferation of
41 squeezed cells for several days[20]. Here, based on the compatibility of this assay with *in-situ*
42 immunostaining and time-lapse analysis, we explored how the nucleus responds to an imposed
43 deformation for several days in a colorectal cancer cell model (HT-29). As expected, within a short
44 timeframe, an unfolding of the nuclear envelope and the appearance of nuclear blebs were observed.
45 Under prolonged confinement, we evidenced for the first time a global nuclear adaptation, with a
46 decrease in nuclear volume within 24 h, and a readjustment of nuclear shape, namely the disappearance
47 of blebs and refolding of the nuclear envelope. Surprisingly, all these changes were triggered by mitosis
48 in a contractility-dependent manner and were conserved by the next daughter's generation, setting a
49 new state of homeostasis.

50 Results

51 Multi-height soft confiner

52 Cells were confined using the agarose-based confiner previously published [20]. In this system, a 2%
53 agarose pad presenting an array of pillars with a height smaller than that of the cell enabled precise cell
54 squeezing. All experiments were performed using agarose exhibiting a stiffness of 150 kPa [20]. In this

55 stiffness range, it is not possible for cells to deform the confining agarose gel. The method originally
56 published by Prunet et al. [20] relied on standard photolithography processes to create the wafers needed
57 for agarose molding, and could only confine cells at a single height per system. We have now upgraded
58 this soft confiner by implementing the possibility to submit a cell population to multiple confinements
59 simultaneously. For that, we developed a multi-height micro-milled mold (Figure 1a), allowing us to
60 control the height of the pillars with a micron resolution. We can confine cells at four different heights
61 within the same system, with a central control zone included, where no confinement was imposed. Each
62 pillar with a given shape corresponds to a specific height: 9 µm (the highest pillar with the least
63 confinement), 7 µm (intermediate confinement), 5 µm (strong confinement) and 3 µm (the strongest
64 confinement) (Figure 1b-c). This multi-height mold was reproducible over time, as illustrated in Figure
65 1d, where the heights of stained cells/nuclei measured at 2 h and 24 h were almost identical. Moreover,
66 cells were properly and homogenously confined within each zone, and displayed the following average
67 heights: 15 ± 0.13 µm for control condition, 8.7 ± 0.45 µm (slight confinement), 6.9 ± 0.16 µm
68 (intermediate confinement, twice the cell size), 5.1 ± 0.13 µm (strong confinement), to 3.7 ± 0.25 µm
69 (very strong confinement, below a fourth of the original cell size) (Figure 1d-e). These cellular heights
70 corresponded to a decrease in nuclear height from 10 ± 0.10 µm (control condition) to 5.9 ± 0.08 µm
71 (slight confinement), 4.9 ± 0.10 µm (intermediate confinement), 3.9 ± 0.04 µm (strong confinement), 2.9
72 ± 0.08 µm (very strong confinement) (Figure 1d-e).
73 Hence, by modifying the soft confiner we previously designed, we obtained a user-friendly, robust, and
74 time-saving system to visualize and analyze the long-term effect of four levels of cell confinement on
75 cancer cell morphology and biology.

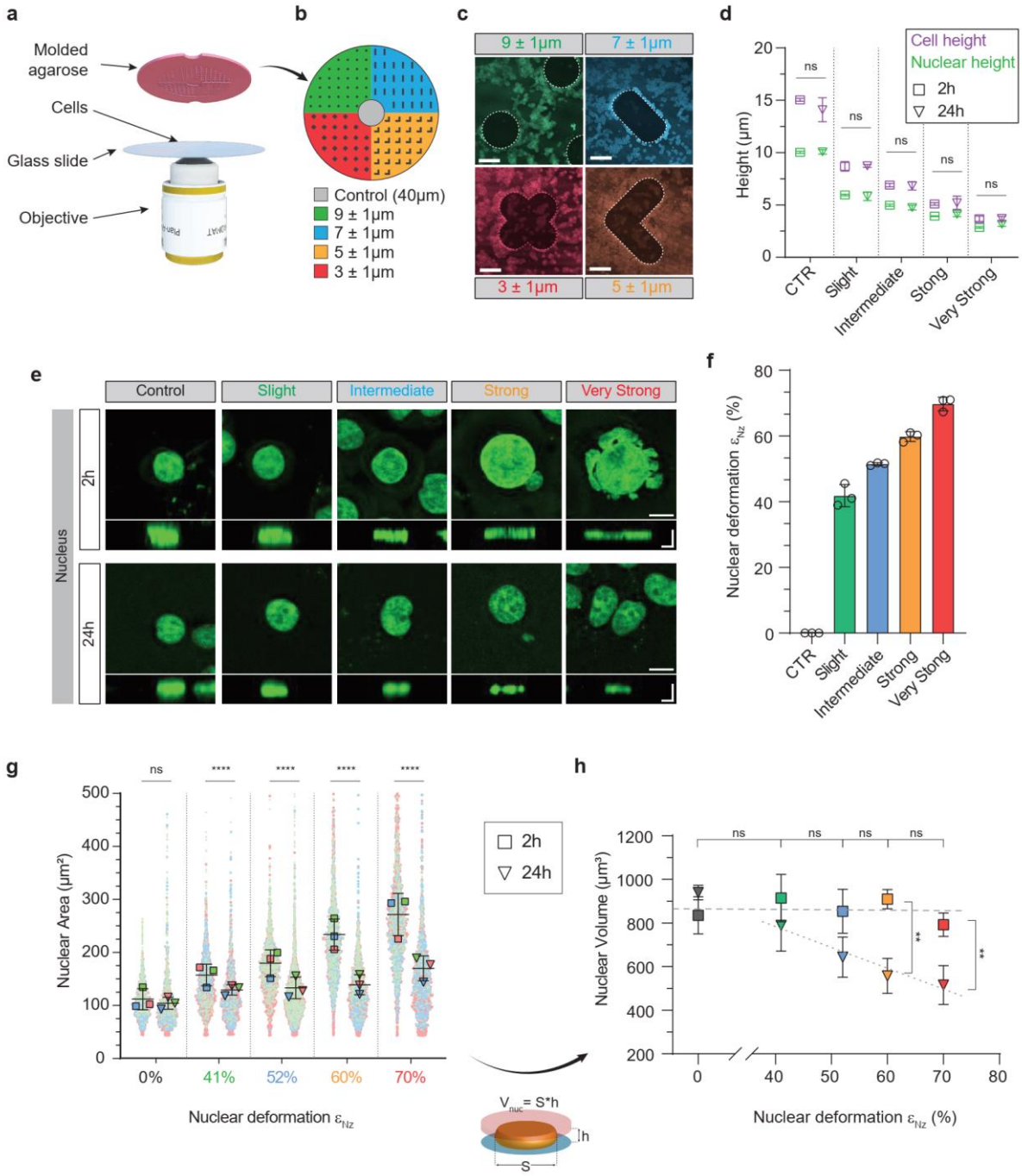

Figure 1: Nuclear volume is regulated according to the level of confinement

(a) 3D representation of confinement principle showing the molded agarose pad. **(b)** Schematic diagram of the multi-height pad with the theoretical heights of each pillar. **(c)** Confocal images of cells and the shaped pillar of each confined zone. *Scale bar = 250 µm*. **(d)** Quantification of cells and nuclear height by z-stack confocal imaging, under each confined zone. *N = 3 experiments with n = 30 cells; Mann-Whitney test*. **(e)** Representative confocal images of nuclei stained with NucGreen in XY (*Scale bar = 10µm*) and its orthogonal view (scale bar = 5µm) at 2 h and 24 h under each level of confinement. **(f)** Nuclear deformation in percent for each degree of confinement defined as $\varepsilon_{Nz} = \left(\frac{h_{nuc}^{ctr} - h_{nuc}}{h_{nuc}^{ctr}}\right) x100$. **(g)** SuperPlot quantifying the projected nuclear area. In each condition, the 3 colors represent 3 distinct experiments with their respective individuals and average value represented by small and large dots respectively. *N = 3 experiments with n > 5,000cells/experiments; Welch's test. Welch's ANOVA test was also performed between each confined condition at 24 h and was not significant*. **(h)** Nuclear volume quantification. *N = 3 experiments with n>5,000cells/experiments; Welch's test. Ordinary one-way ANOVA was carried out between each confinement condition at 2 h and was not significant*.

Long-term nuclear volume regulation

Having optimized the confinement system, we then investigated how long-term confinement affects cell nuclei. We first computed the nuclear deformation for each level of confinement (Figure 1f) and obtained a nuclear deformation along the z-direction (ε_{Nz}) of 41 ± 3% for slightly confined cells, 52 ± 0.5% for an intermediate confinement, 60 ± 1% and 70 ± 2% for strong and very strong levels of confinement, respectively (Figure 1f). These deformations are associated with changes in nuclear projected-area and nuclear volume. At 2 h of confinement, the nuclear-projected area increased with the level of confinement (Figure 1e-g), while the volume of each nucleus, computed by approximating the shape of the nucleus to a cylinder (See schematic representation in Figure 1g), remained constant for all imposed deformations (Figure 1h, squares). Intriguingly, at 24 h of confinement, the nuclear-projected area of confined cells decreased towards that of the control condition (Figure 1g, triangles). This decrease in nuclear-projected area corresponds to a proportional decrease in nuclear volume after 24 h of confinement (Figure 1 h, triangles), with a nuclear volume loss from 20 ± 6 % (for slight confinement), 25 ± 7 % (for intermediate confinement), 39 ± 8% (for strong confinement) to 34 ± 15 % (for very strong confinement, Supplementary Fig. 1a). Interestingly, this loss in nuclear volume was inversely proportional to nuclear deformation ε_{Nz} (Figure 1h, dotted line).

In addition, the distance between the cell membrane and the nuclear envelope was significantly reduced with confinement (Figure 1d, Supplementary Fig. 1c) and accompanied by the re-localization of the contractility machinery (Phosphorylated Myosin Light Chain (p-MLC) staining) from above the nucleus to the lateral plane indicating a cortex rearrangement (Supplementary Fig. 1d).

Moreover, at 2 h of cell confinement, DNA damages appeared as evidenced by an increase in the number of γH2AX foci (marker of double-strand breaks, Supplementary Fig. 1e-f) per cells. This confinement-induced DNA damages was repaired at 24 h, as the number of foci per cells in confined conditions was identical to that of unconfined ones (Supplementary Fig. 1e-f).

114 ## Long-term regulation of nuclear tension

115 Under the strongest levels of confinement (60% and 70% nuclear deformation), we observed nuclear
116 protrusions at 2 h (Figure 1e, strong-very strong confinement panel and Figure 2a), which participated
117 in the increase in nuclear-projected area, though not entirely as the increase remained significantly
118 different even if protrusions were dismissed to compute the projected area (Supplementary Fig. 1b). As
119 observed, the nuclear volume remains constant for short timescales (2 h), but due to the applied
120 confinement and geometrical considerations, the nuclear envelope (NE) unfolds, its tension increases [21],
121 which can lead to nuclear protrusions [22–24]. Nuclear protrusions are dynamic structures whose
122 membrane can rupture – visualized by leakage of NLS-RFP dye to the cytoplasm (Supplementary Fig 2a,
123 arrows) – and repair[17].

124 The proportion of nuclei displaying protrusions (indiscriminately called blebs in the rest of the
125 manuscript for simplicity), as well as dividing, apoptotic and normal nuclei was quantified according to
126 their morphology (Figure 2a, insets). Under slight confinement (41 % nuclear deformation), blebbing
127 nuclei represented only 4.2 ± 4.7 % of all nuclei (Figure 2b). However, the proportion of these nuclei
128 gradually increased with the degree of confinement and represented 37.7 ± 6.7 % and 63.4 ± 11.8 % of
129 all nuclei for 60% and 70% of nuclear deformation, respectively (Figure 2b). Strikingly, at 24 h of
130 confinement, those proportions dropped to less than 10 %, which was reflected by an increase in normal
131 nuclei proportions (Figure 2c-d). The number of blebs per cell and the size of those blebs were also
132 drastically reduced at 24 h under strong confinement (Supplementary Fig. 2b-e). This change in nuclear
133 phenotype at 24 h is in accordance with the reduction in nuclear volume and the refolding of the nuclear
134 envelope. Nuclear envelope folding was quantified from lamin A/C immunostained images with the
135 positive area defined as the excess area of the lamina envelope compared to the nuclear area (See
136 methods and schematic representation in Figure 2f). In control conditions, the nuclear envelope was
137 folded, reaching similar levels at 2h (56 ± 1.5%) and 24h (57 ± 2%) (Figure 2e-f). Under a strong level of
138 confinement (60% nuclear deformation), a complete unfolding of the nuclear envelope was observed at
139 2 h, evidenced by a radical decrease of the positive area (Figure 2e-f, down to 20 ± 1 %). Strikingly, at 24

h, a refolding of lamin A/C was observed (Figure 2e), with an increase in the positive area (34 ± 1 %) (Figure 2e-f).

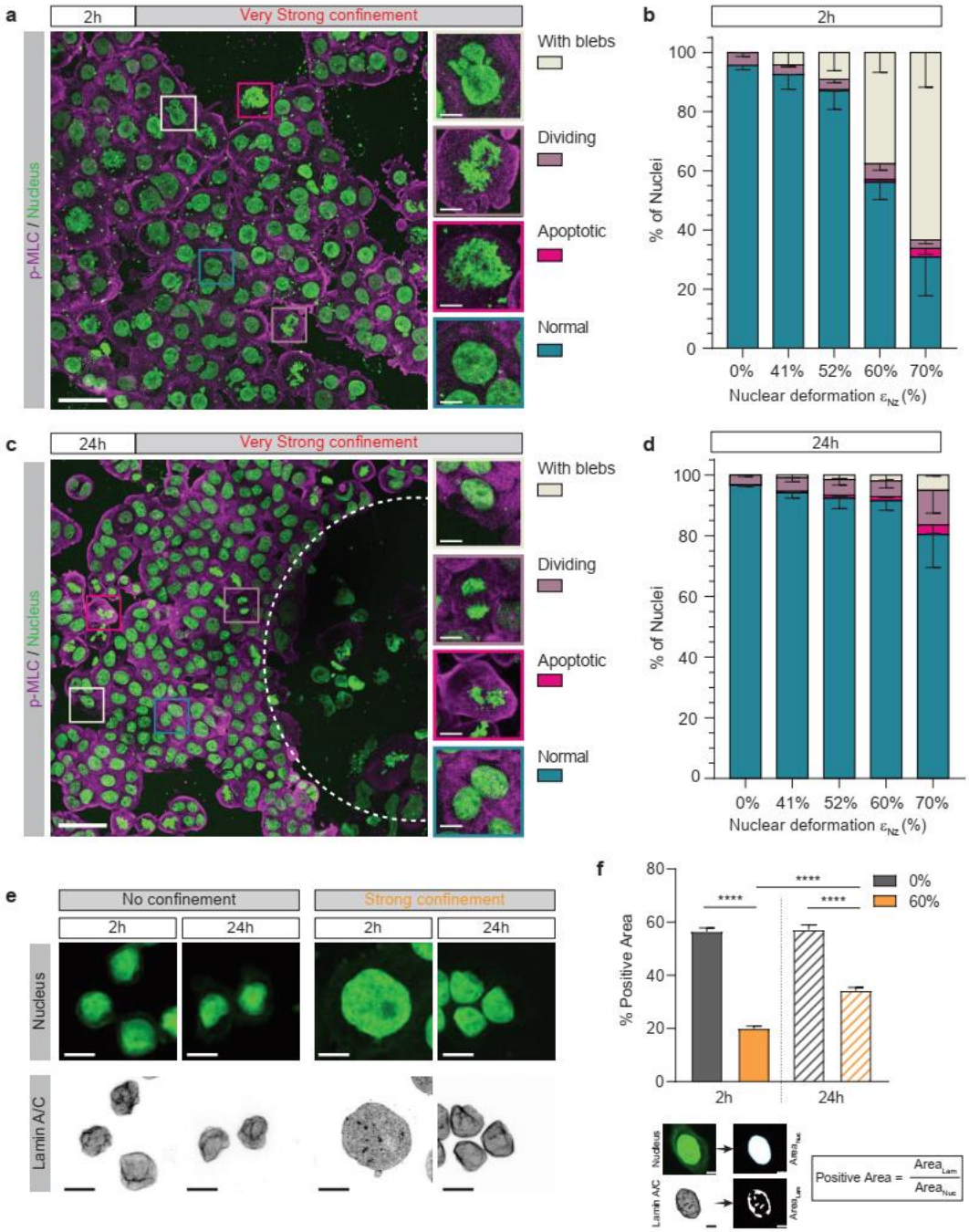

Figure 2: Regulation of nuclear tension

(a, c) Max projection confocal images of stained nuclei and pMLC at 2 h and 24 h, respectively, scale bar = 50 µm. Cropped nuclei correspond to nuclei with blebs, dividing and apoptotic cells and normal nuclei, at 2 h (a) and 24 h (c), scale bar = 10 µm. **(b, d)** Percentage of HT-29 cells presenting nuclear blebs, dividing, apoptotic cells, or normal nuclei in control condition or under confinement, at 2 h **(b)** and 24 h **(d).** *N = 3 experiments with n > 5,000cells/experiments.* **(e)** Representative confocal images (max intensity projection) of stained nuclei and lamin A/C without confinement (control) or under 60% nuclear deformation (strong confinement) at 2 h and 24 h. *Scale bar = 10 µm*. (f) Quantification of the positive area of the nuclear envelope (lamin A/C) which represents the folded nuclear envelope. *N = 3 experiments with n > 30cells/experiments; mean ± SEM; Mann-Whitney test*.

152 Thus, not only was nuclear volume regulated at 24 h of confinement but also nuclear blebbing, and
153 nuclear envelope folding, suggesting either a relaxation of the nuclear envelope tension, either an
154 inability of cells with blebs to divide. All these changes (volume decrease, blebs disappearance, nuclear
155 envelope refolding) are referred as global "nuclear adaptation" in the rest of the manuscript.
156 In addition, we noticed a constant proportion of dividing cells at 24 h of confinement below 60% of
157 nuclear deformation, albeit a slight increase at 70% nuclear deformation (Figure 2c-d). This increase in
158 dividing nuclei was most likely due to an increase in the duration of mitosis (Supplementary Fig. 3a),
159 already described by Lancaster et al. [10].

160 Cell cycle progression does not explain long-term nuclear adaptation

161 We next performed experiments to narrow the range of potential mechanisms involved in this long-term
162 nuclear adaptation. To this end, we conducted time-lapse experiments on live cells by confining HT-29
163 expressing the FUCCI fluorescent cell cycle reporter system over 3 to 4 days (Figure 3a). We first,
164 hypothesized that an alteration of cell cycle progression could explain the loss of nuclear volume
165 observed under prolonged confinement. It was reported that mechanically confined cell, without having
166 the possibility to round up for division, results in stressed cell division with delayed mitosis, multi-
167 daughter mitosis events, unevenly sized daughter cells and induction of cell death[9,10]. We confirmed this
168 experimentally and saw a gradual increase in abnormal divisions with the level of confinement, from
169 none for control conditions to 40 ± 4% for very strong confinement (Supplementary Fig. 3b,
170 Supplementary Movie 1). In addition, for mother cells, while the duration of the first mitosis was similar
171 for control and slight confinement (Supplementary Fig. 3a, respectively 1.8 ± 0.1 h and 1.6 ± 0.1 h), it
172 doubled for cells under strong confinement (3.5 ± 0.4 h), and considerably increased up to 9.2 ± 0.8 h for
173 very strong confinement, reaching up to 20h in some cases (Supplementary Fig. 3a). The time spent in
174 G2 for mother cells also increased for cells under very strong confinement (Supplementary Fig. 3c), and
175 led to a larger increase in volume during this S-G2-phase (Supplementary Fig. 3d), with no significant
176 increase in volume detected before the G2-phase (Supplementary Fig. 3e).

177 We then focused on the cell cycle taking place after a first confined division. Surprisingly, for the
178 daughter cells, we found that confinement did not significantly change the duration of the whole cell
179 cycle (Figure 3b) and neither that of its subpart (G1, S-G2 Supplementary Fig. 3f). Indeed, the entire cell
180 cycle for daughter cells lasted 27 ± 7 h under slight confinement, 23 h ± 4 under strong confinement
181 compared to 22 ± 5 h under no confinement (Figure 3b). Similarly, relative nuclear growth (change in
182 volume normalized by their initial volume) remained unchanged under confinement during the entire
183 cell cycle (Figure 3c), and during its subpart (Supplementary Fig. 3g). Likewise, nuclear growth rates of
184 confined cells were similar regardless of the level of confinement (Figure 3d), with no significant
185 difference in its subpart (Supplementary Fig. 3h). These results suggest that long-term nuclear volume
186 regulation of daughter cells cannot be explained by changes during cell cycle progression nor growth
187 rate.

188 ## Long-term nuclear adaptation occurs during confined mitosis

189 We then focused on changes of nuclear volume during confined mitosis. A reasonable assumption is that
190 the nuclear volume is conserved throughout mitosis, so that the volume of the sum of the two daughter
191 cells after division is equal to the volume of their mother cell. Intriguingly, nuclei were smaller after the
192 first division under confinement (Figure 3e-f), with a volume ratio decreasing gradually with increasing
193 nuclear deformation, similarly to the one observed at 24 h on fixed samples (Figure 1h, 3f and
194 Supplementary Figure 3i for the fit). The loss of volume during mitosis reached up to 60 ± 15% for the
195 strongest confinement (Figure 3f). The fact that we obtain the same proportionality on both fixed (Figure
196 1h) and live (Figure 3f) experiments confirm the robustness of our results concerning such nuclear size
197 regulation. On the contrary, during the second division under confinement, we observed no volume loss
198 (Figure 3f, generation 2). Hence, the nuclear volume seems to have reached homeostasis after the first
199 confined division and does not shrink further during a second confined division. Therefore, mitosis
200 appears to be the main checkpoint in the observed long-term adaptation of nuclear volume.

201 This prompted us to investigate whether mitosis could also play a role in the loss of nuclear blebs. Using
202 time-lapse experiments, we quantified the nuclear blebs before and after confined divisions (Figure 3g-

203 h). Before mitosis, the mean number of blebs per cell was 1 ± 0.3 for cells under strong confinement
204 (Figure 3h, 60% nuclear deformation), and reached 3 ± 2.2 for very strong confinement (Figure 3h, 70%
205 nuclear deformation). However, immediately after mitosis, the mean number of blebs per cell was close
206 to 0 for both strong and very strong confinement (Figure 3g-h, Supplementary Movie 2). In addition, we
207 observed no blebs before the second mitosis (Figure 3h). We can thus conclude that the loss of nuclear
208 blebs is essentially due to cells undergoing mitosis, suggesting that nuclear volume and nuclear envelope
209 tension are tightly coupled, and supporting the hypothesis that mitosis is a key regulator of nuclear
210 envelope tension.

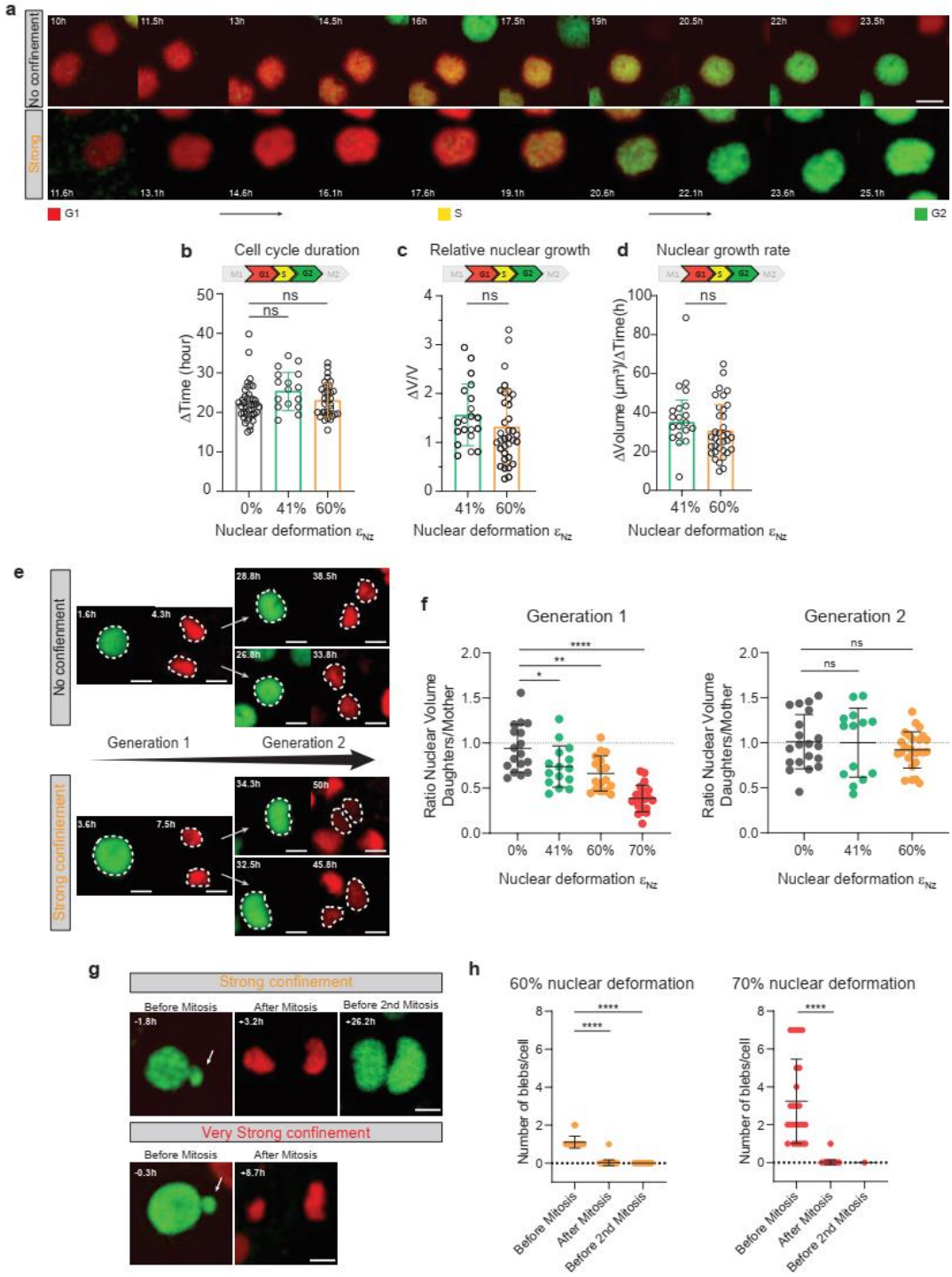

Figure 3: Global phenotypic regulation of the nucleus occurs through mitosis

(a) Time-lapse images of HT-29 nuclei expressing the FUCCI fluorescent cell cycle reporter, without confinement (control) or under strong confinement (60% nuclear deformation). *Scale bar = 10 µm*. **(b, c, d)** Quantification of the duration **(b),** the relative nuclear growth **(c)** and the nuclear growth rate **(d)** of HT-29-Fucci cells under several levels of confinement during an entire cell cycle after the first cell division. *N = 2 experiments with n > 200 cells, Mann-Whitney test for (b, c), and unpaired t-test for (d)*. **(e)** Representative images of nuclei at the end of the G2 phase (just before mitosis) and its respective daughter nuclei just after mitosis (beginning of G1 phase), following two consecutive divisions, for control and strong confinement conditions. *Scale bar = 10 µm*. **(f)** Quantification of the size of daughter nuclei over their respective mother following two consecutive divisions, under several levels of confinement. *N = 2 experiments with n = 130 cells, unpaired t-test*. **(g)** Sequential images of a blebbing nucleus under strong or very strong confinement before and after mitosis, NEB is set here as a reference time t = 0 h. *Scale bar = 10 µm*. **(h)** Quantification of the number of blebs before and after mitosis under strong and very strong confinement. *N = 3 experiments with n = 167 cells, Mann-Whitney test*.

224 ## Adaptation of nucleus phenotype and volume is contractility-dependent

225 Acto-myosin contractility is a well-known transducer of stress to the nucleus, inducing deformation and
226 blebbing [22]. Conversely, it has been shown recently that nuclear tension and blebbing increase cell
227 contractility [15,16]. Therefore, to gain further insights into the mechanisms involved in this global nuclear
228 adaptation, we inhibited cell contractility using Blebbistatin, a pharmacological inhibitor of myosin II.
229 The addition of Blebbistatin immediately after confining cells, imped nuclear volume regulation, as
230 evidenced at 24 h under very strong confinement (Figure 4a-b). Of note, while at 2 h under very strong
231 confinement (70% nuclear deformation) the number of nuclear blebs drastically increased with or
232 without the addition of Blebbistatin (Figure 4c, 2 h), very few blebs had disappeared at 24 h with
233 Blebbistatin (Figure 4c, 24 h and Supplementary Fig. 4d). Similarly, inhibiting contractility before applying
234 the confinement (Blebbistatin added 1h before confinement) also prevented the regulation of nuclear
235 volume and blebs (Supplementary Fig. 4 a-c).

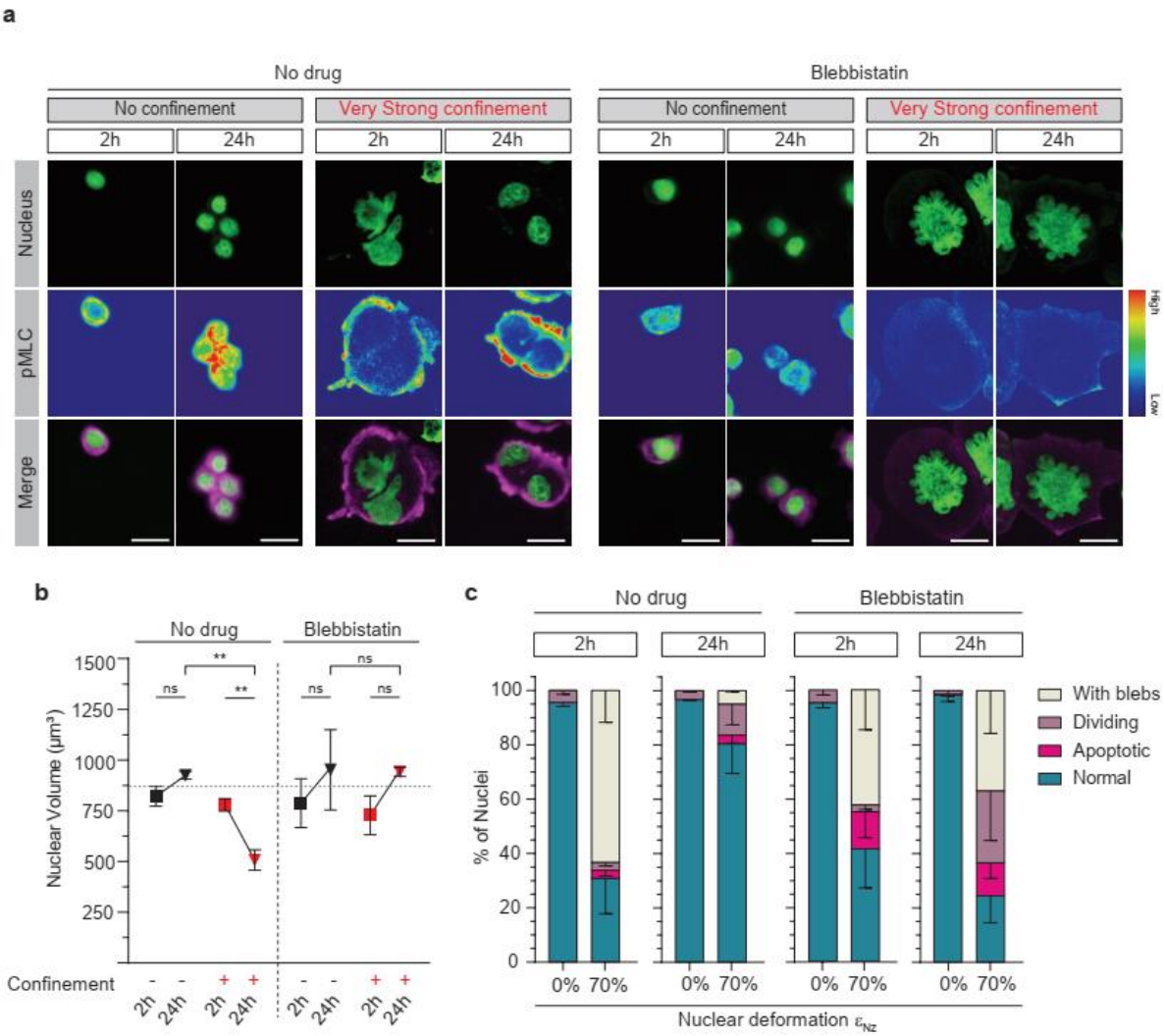

Figure 4: Contractility is essential for nuclear regulation

(a) Representative images of stained nuclei and phospho-Myosin Light Chain either with or without Blebbistatin at 2 h and 24 h, without confinement or under very strong confinement. *Scale bar = 20 µm*. **(b)** Quantification of nuclear volume at 2 h and 24 h with or without Blebbistatin, without confinement or under very strong confinement. *N = 3 experiments with n=9,818 cells, mean ± SEM, unpaired t-test (for no drug conditions) or Mann-Whitney test (for Blebbistatin conditions).* **(c)** Quantification of nuclei with blebs, dividing, apoptotic, or normal without confinement or under very strong confinement at 2 h and 24 h, with no drug or with Blebbistatin. *N = 3 experiments with n = 9,818 cells.*

Cells regulate their apparent nuclear surface during mitosis

From our data, we calculated the apparent surface of confined nuclei S_{app} (See Supp. Mat 1), which corresponds to the surface of a cylinder. As expected, the apparent surface passively increases after 2 h under confinement, while it seemed to remain constant at 24 h (Figure 5a). Moreover, this constant apparent surface was similar for non-confined cells. This strongly suggests that the apparent surface is the key parameter regulated during prolonged confinement.

To test whether it is the total surface of nuclear envelope that determines the nuclear volume, we estimated the surface for unfolded nuclear envelope conditions after 2 h under confinement S_0 (See Supp. Mat. 1). From S_{app} (apparent surface) and S_0 (total surface, obtained in the unfolded nuclear envelope condition) we computed the expected nuclear volumes in confined conditions (Figure 5b) and found that the volumes calculated using S_{app} were in good agreement with the experimental volumes measured after 24 h under confinement (Figure 5c). Collectively, these geometrical arguments strongly suggest that the nuclear volume is not limited by the total surface of the nuclear envelope available, but rather actively set by the apparent surface that remains constant under different geometrical constraints.

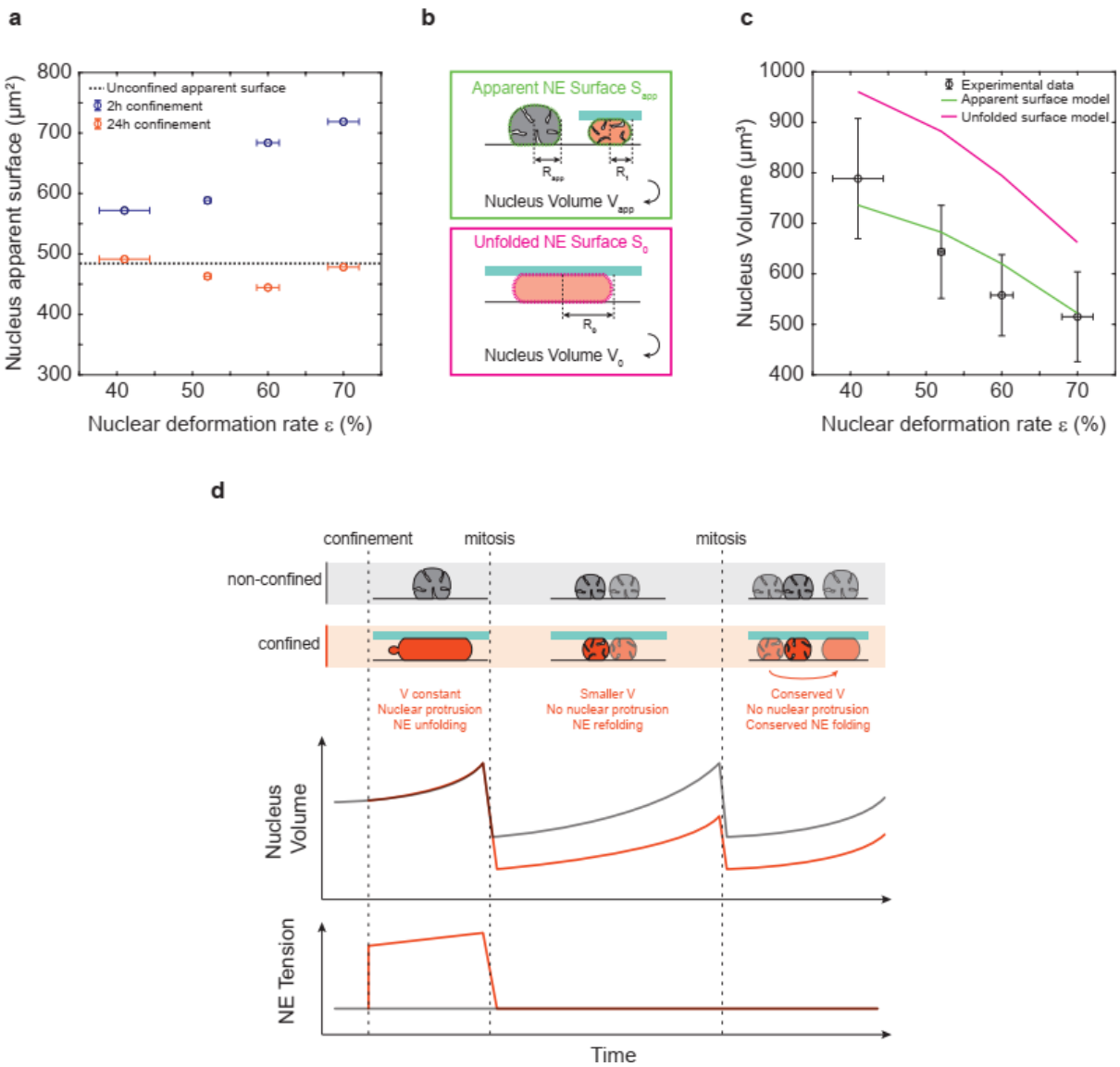

Figure 5: Nuclear total surface determines the final nuclear volume

(a) Nuclear apparent surface as a function of the deformation ε_{NZ} at 2 h and 24 h under confinement. The dashed line shows the apparent surface measured for unconfined cells. **(b)** Schematic representation of the geometric model, showing the apparent nuclear envelope surface S_{app} and the unfolded nuclear envelope surface S_0 **(c)** Calculations of nuclear volume using the apparent surface (green) and the total surface (pink). The total surface is obtained from the tensed nuclear envelope measured under intermediate confinement at 2 h. Experimental values are shown in black. **(d)** Diagram summarizing the results showing that under confinement before mitosis, the nuclear envelope is tensed and tension increases as evidenced by the nuclear blebs. Tension is then released during the first mitosis as the nuclear volume is lower at mitosis exit. Low initial tension is restored, nuclear-envelope folds appear again but not blebs.

274 ## Discussion

275 Deciphering how the nucleus reacts to long-term confinement is of primary importance in the context
276 of cancer progression and response to treatment [25,26]. Using an imposed deformation, we show that the
277 nucleus is regulating both its volume and its structure (blebs, lamin A/C folding) within 24 h. We
278 evidenced that this regulation is mediated by mitosis: nuclei then reach a new state of homeostasis, with
279 no further adaptation observed in the next generations. This regulation is an active process requiring the
280 contractility machinery. In addition, a simple model supports the idea that the total nuclear surface is a
281 key parameter in setting the nucleus size and consequently alleviating nuclear envelope tension (see
282 Figure 5d for a schematic representation).

283 ### Strong confinement increases nuclear envelope tension and growth

284 Taking advantage of the compatibility of our soft-confiner system with time-lapse microscopy, we were
285 able to follow the same cells for several cell divisions and observed different steps of adaptation to
286 various levels of confinement. The first step takes place before the first division of confined cells. Within
287 the first hours of confinement, only highly confined cells display an increase in nuclear growth rate
288 (Supplementary Fig. 3d), in accordance with the nuclear envelope tension threshold observed for HeLa
289 cells[15]. This increase in growth rate might be due to an increase in nuclear import following a rise in
290 nuclear envelope tension and uncoupled nuclear and cytoplasmic volumes as proposed by Pennacchio
291 et al.[27–29]. This bias in nuclear shuttling can generate an increase in nuclear osmotic pressure and account
292 for the blebbing observed during the first hours under confinement (Figure 2a-b)[8,30]. This increase in
293 growth rate is also accompanied by a lengthening of the G2 phase (Supplementary Fig. 3c). Conversely,
294 slighter levels of confinement did not impact cell cycle progression (Supplementary Fig. 3c-e), suggesting
295 that the flattening required for the G1 to S transition observed for HeLa cells[13] should be sufficient to
296 fully extend the nuclear envelope or might be cell type dependent.

297 ## Mitosis plays a key role in nuclear adaptation to confinement and alleviation of nuclear envelope
298 tension

299 The key step in nuclear adaptation to confinement is clearly cell mitosis. We clearly show that the
300 regulation of nuclear volume observed at 24 h of confinement largely originated from volumetric
301 changes at division exit (Figures 1h and 3f). Confined mitosis can be prolonged due to defects in spindle
302 assembly[10] or leads to asymmetric or multi-daughter division[9], but so far such shrinking of the nucleus
303 during division has never been observed to our knowledge. More strikingly, no more shrinking was
304 observed for the second division under confinement (Figure 3f). This important observation points out
305 toward a true adaptation to confinement: once adapted, there is no further volume decrease.
306 So far, however, the mechanisms involved remain elusive. Using a mechanistic approach, we showed
307 that the apparent nuclear surface is the parameter conserved over a long time and therefore during cell
308 division (Figure 5). By regulating the apparent surface of their nucleus, cells can adjust their nuclear
309 envelope tension to a homeostatic level. Indeed, mitosis also plays a pivotal role in relaxing the nuclear
310 envelope tension generated by confinement as nuclear blebs disappeared completely after the first
311 mitosis (Figure 3h), while nuclear envelope folds reappeared in confined conditions at 24 h (Figure 2e-
312 f).
313 Of note, we also observed a population of abnormal divisions (multi-daughter cells, cells blocked in
314 mitosis), as already reported for Hela cells [9,10]. In the future, it could also be of interest to analyze how
315 this abnormal subpopulation regulates (or not) its nuclei.

316 ## The critical role of actomyosin contractility in the regulation of lamina tension and nuclear volume

317 The nuclear adaptation we evidenced was lost by blocking contractility via Blebbistatin treatment. This
318 result is in accordance with the fact that abnormal actomyosin contractility is associated with changes
319 in cell division, such as defects in spindle positioning[10,31], failed mitosis, and the appearance of
320 polynucleated cells [9,10]. During cell division, actomyosin contractility participates in cleavage furrow
321 formation[32]. Here, our results suggest that contractility is required to set nuclear volume and nuclear
322 envelope folding, mostly during nuclear envelope reformation at the end of mitosis.

323 ## Regulation of nuclear repair mechanism associated with lamina folding and nuclear volume loss

324 Consistent with previous studies[33,34], we also evidenced an increase in DNA-damage at 2 h of
325 confinement (Supplementary Fig. 1e-f). Such an increase in DNA-damage could lead to chromosomal
326 instability and mutations[35,36]. However, very interestingly, in addition to lamina refolding and nuclear
327 volume loss, we also observed a decrease in DNA damage at 24 h of confinement (disappearance of most
328 γ-H2AX foci, Supplementary Fig. 1e-f). This is in accordance with the reported role of lamin in the DNA
329 damage repair pathway [37] and a lower nuclear envelop tension associated with bleb disappearance. Such
330 repair mechanisms have also been reported in other confinement situations [18], as well as in response to
331 other stresses like radiotherapy [38]. As such repair mechanism is highly correlated with cell-cycle re-entry
332 [18], this is again consistent with a key role for mitosis in such DNA-damage regulation in response to
333 nuclear deformation.

334 Growing evidence also indicates a role for lamins in the regulation of transcription [39], replication, and
335 genome stability [40]. It will be very interesting to further investigate the effect on transcription activity,
336 protein synthesis, as well as chromatin condensation.

337 ## Conclusion and outlooks

338 Here, under prolonged cancer cell squeezing, we experimentally highlighted the critical role of mitosis
339 in the regulation of nuclear envelope lamina folding, nuclear blebs, and nuclear volume. Using simple
340 geometric assumptions, we show that homeostasis of nuclear volume is set by the apparent surface of
341 the nuclear envelope.

342 This study calls for in-depth analysis of the molecular pathways at play, as well as for deciphering the
343 consequences that such regulation could have in the context of cancer and resistance to therapies. We
344 anticipate the role of calcium as well as cPLA2, both of which were recently reported to be involved in
345 nuclear deformation sensing [15]. The nuclear to cytoplasmic ratio, which is constant within a given
346 population, is most likely to be impacted by the confinement and changes in nuclear envelope tension
347 [27,41,42], and might be at play in the regulation we describe herein. The import/export regulated by the
348 nuclear pore complex is also a putative important player [28]. Lastly, we identified a clear change in lamin

349 unfolding/refolding during this nuclear adaptation: lamins and lamin-associated proteins are known
350 regulators of nuclear size [42] and should therefore be further investigated, especially in the context of
351 cancer.

352 Noteworty, as already mentioned, the agarose gel used herein exhibit a stiffness of 150 kPa[20], which is
353 too rigid for the cell to deform the gel. It would be interesting in the future to analyze cell response using
354 softer gels (in the kPa range). Indeed, if the cells are able to deform the gel, the nuclear regulation
355 highlighted in this study could be completely different. In Lancaster et al. [10], when the mitotic cells were
356 able to deform the gel, they divide normally.

357 Outlook in the context of cancer

358 Abnormal nuclei shape [43], together with alterations in the expression of lamin A and lamin B is a hallmark
359 for the prognosis of many tumors [25], including colorectal cancer [44]. Low lamin A/C is associated with a
360 decrease in stiffness, irregular shape, and larger nuclei deformation [45] as well as increased metastatic
361 capacities [46]. Noteworthy, the HT-29 cell line used in this study presents the p53 mutation [47], has no
362 lamin B2, and low lamin B1 level [48]. Loss of lamin B1 leads to nuclear blebs, while it has been reported
363 that nuclear envelope rupture is dependent on p53 [49]. To gain further insight into the role of lamins and
364 p53 mutations in nuclear regulation we evidenced in this study, it would be interesting to analyze nuclear
365 adaption in response to prolonged confinement in other cancer cell lines of different origins, as well as
366 in colorectal cancer cell lines of higher grades, with no p53 mutation and/or exhibiting different levels
367 of lamins expression.

368 Potential implications for drug resistance of cancer cells

369 The regulation of nuclear size identified in this study could have important consequences on resistance
370 to classical chemotherapeutic treatment targeting proliferation. In addition, emerging pharmaceutical
371 compounds specifically targeting nuclei size are currently under investigation (Nuclear Size Rectifiers[50]).
372 Deciphering the molecular pathways involved in such nuclear regulation and more specifically the inner
373 nuclear membrane re-assembly post-mitosis [51,52] could pave the way towards novel therapeutic

374 strategies. Finally, our soft confiner is an ideal tool for identifying cancer drug targets as it allows users
375 to test several conditions simultaneously.

376 Material and methods

377 Cell culture

378 HT-29 wild type colorectal adenocarcinoma cells were purchased from the ATCC (HT29 HTB-38). A stable
379 cell line expressing NLS-mKate2 was established using the lentiviral vector IncuCyte® nuclight orange
380 (λex=555nm, λem=584nm): the cells were selected using puromycin according to the manufacturer
381 protocol. The stable HT29 expressing Fucci (Cdt1-RFP and hGeminin-GFP) cell line was a gift from Dr.
382 Toufic Renno's team (CRCL, Lyon, France).
383 All cells were cultured in Dulbecco's modified Eagle's medium (DMEM - Glutamax, Gibco™)
384 supplemented with 10% heat-inactivated fetal bovine serum (FBS; PanBiotech™), 100 units/100µg
385 penicillin/streptomycin (Gibco™). Routinely, all HT-29 cell lines were grown in T-25 cell culture flasks
386 and kept at 37°C and under 5% CO_2. Culture medium was changed regularly, and cell passage was carried
387 out at 70% confluency. Cell lines were tested for Mycoplasma every 6 months and the tests were
388 negative.

389 Drug treatments

390 The following pharmacological inhibitors and chemical compounds were used: Blebbistatin (Tocris™) at
391 a final 100 µM concentration.
392 To inhibit cell contractility before confinement, we added 500µL of medium with 100µM blebbistatin 1h
393 prior confinement.
394 To inhibit cell's contractility after confinement, 500 µL of medium solution with 200 µM of Blebbistatin
395 was added following the confinement (to reach a final concentration within the confiner of 100 µM).
396 Initial rinsing after confinement was also made with medium containing Blebbistatin at 100 µM.

397 Multi-height micro-milled mold fabrication

398 The height of the micropillars (from 9 µm to 3 µm) determines the level of spatial confinement of cells.
399 The array presents regularly distributed pillars (distance between each pillar of 800µm) with specific

400 shapes according to their height: the “o” shape for 9 µm; the “-” shape for 7µm; the “L” shape for 5 µm;
401 the “+” shape for 3µm. The field of pillars is surrounded by a solid band of 3.5 mm to stabilize the
402 structure, and two external notches to enable the proper positioning during molding. The pillars were
403 drawn using Autodesk software and the mold was created using the CNC Mini-Mill/GX on brass.

404 ## Microfabrication-based confinement of cell populations

405 Cell confinement was performed using the agarose-based soft cell confiner methods previously
406 described [20] and now available as Agarsqueezer (https://www.idylle-labs.com/agarsqueezer-by-
407 softconfiner). All cell lines were seeded in the systems overnight before confinement on glass coverslips
408 previously coated with fibronectin 50 µg/mL (Sigma-Aldrich™) (1h incubation in the system at room
409 temperature and washed 3 times with PBS). All the cell lines were seeded at the same intermediate cell
410 density level: 500 µL of a cell solution at 180,000cells/mL.

411 ## Agarose molding

412 Based on the procedure described in Prunet et al.[20], molding was adapted to obtain accurate agarose-
413 replicates from the newly developed multi-height brass mold. First, a solution of agarose diluted in
414 distilled water (2% (w/v)) was prepared by autoclaving at 120 °C for 10 min, or 30 s microwave (1000 W).
415 All the following steps were performed under a sterile culture hood, and the polycarbonate (PC) holder
416 was UV sterilized before use (20 min on each side under 24 W, 365 nm). 400 µL of the prepared agarose
417 solution was deposited in the prewarmed PC holder (placed on a hot plate at 75°C) and was left at room
418 temperature for 5 min to let it gel. Then, 500 µL of the prepared agarose solution was deposited on the
419 prewarmed micro-milled brass mold (on the same hot plate temperature) with the PC holder and placed
420 under the press (Supplementary Fig. 5). The press generates a uniform pressure and ensures the contact
421 between the PC holder and the mold, to ensure proper molding and resolute pillars. After 30 min under
422 press at room temperature, the PC holder was gently removed from the brass mold. Evenly distributed
423 holes were drilled into the gel using a 20G and 16G puncher and through holes present on the PC holder.
424 In total, five 16G holes and four 20G holes were done. The molded agarose gel was then placed in sterile
425 PBS and sterilized under UV light (20 min on each side). The molded agarose can be stored in its PC

426 holder at 4°C in PBS until further use. It was replaced either by culture medium or by drug treatment and
427 incubated at 37 °C at least 12h before the confinement experiment.

428 Immunostaining

429 During confinement, cells were fixed *in situ* with paraformaldehyde (PFA): cell culture medium was
430 removed, and cells were washed twice with PBS. 4% PFA (Electron Microscopy Sciences™) was added
431 and incubated for 40 min at RT. After incubation, samples were rinsed with PBS - 3% BSA (Sigma-
432 Aldrich™) (3x20min). The agarose gel is then removed and cells were permeabilized using 0.5% Triton X-
433 100 (Acros Organics™) for 10 min at RT. After blocking with PBS - 3% BSA (3x5min) to inhibit non-specific
434 binding of antibodies, cells were incubated overnight at 4°C with primary antibodies diluted in PBS - 2%
435 BSA - 0.1% Triton X-100. After 3x5min washes with PBS, samples were incubated with secondary
436 antibodies for 2 h at RT. The primary antibodies used were: p-MLC (Cell signaling™ at 1/50); LaminA/C
437 (Santa Cruz Biotechnology™ at 1/100), γH2Ax (Santa Cruz Biotechnology™ at 1/200). NucGreen™ Dead
438 488 (Invitrogen™, 1 drop per 3 ml in PBS); Alexa 647 Phalloidin (Invitrogen™ at 1/500); Alexa 555
439 Phalloidin (Invitrogen™ at 1/500) were also used. The secondary antibodies used were: Anti-Mouse 647
440 (Invitrogen™ at 1/500); anti-rabbit 647 (Invitrogen™ at 1/500), anti-mouse 555 (Invitrogen™ at 1/500).
441 Coverslips were then mounted using 2 drops of Fluoroshield™ (Sigma-Aldrich™) and varnish-sealed after
442 overnight hardening at room temperature.

443 Confocal fluorescence microscopy

444 Fixed samples were visualized using a Leica SP5 confocal microscope with a 20x Dry objective (NA = 0.65),
445 a 40x oil immersion (NA = 1.25), a 40x Dry (NA = 0.95) or a 63x oil immersion (NA = 1.25) objectives.
446 Images were collected in sequential mode using averaging at a resolution of 1024x1024. Z-stacks of cells
447 were acquired to precisely measure the height of confinement and nuclear volumes (dz = 0.2 µm or 0.5
448 µm for each stack).

449 Epifluorescence imaging

450 Fixed samples were also visualized using an inverted microscope Leica DMI8 using epifluorescence
451 microscopy with a 40x dry objective (NA = 0.55).

452 ## Live-cell imaging

453 Cells were observed with an inverted microscope Leica DMI8 using epifluorescence imaging. Timelapse
454 imaging was performed for 2 to 5 days in a controlled environment (CO_2, temperature, and humidity),
455 using a 20x dry objective (NA = 0.65). A motorized x-y stage enabled the concomitant recording of up to
456 20 regions for each system every 10 min.

457 ## Quantitative image analysis

458 **Cell height, nuclear area, and volume** were assessed with a homemade routine workflow using both
459 ImageJ/Fiji and MATLAB® software. First, after applying a gaussian blur on nuclei-stained images, nuclei
460 were automatically detected either using the stardist Fiji plugin [53] or using the Otsu's threshold detection
461 directly in Matlab®. Mask and labeled images obtained were exported in Matlab® to perform automated
462 morphological analyses on individual pre-labeled nuclei. The Z-plot profile of ImageJ/Fiji was used on
463 orthogonal views of both nuclei and phalloidin staining to obtain nuclear and cell heights, respectively.
464 Codes are available upon request.

465 For the nuclear area, at least four different areas were imaged and analysed per conditions.

466 **DNA compaction** was determined by measuring the fluorescence intensity levels of NucGreen –a DNA
467 intercalant – on an inverted epifluorescence microscope (Leica DMI8), and normalized by the height of
468 nuclei.

469 **Proportion analysis of nuclear blebs** both in live and fixed experiments was conducted using the cell
470 counter plugin of ImageJ/Fiji. To further characterize the nuclear blebbing phenotype, labeled images of
471 nuclei and their blebs were obtained using the stardist Fiji plugin [53] (blebs are automatically extracted
472 from the main nuclei using stardist) We filtered the core nucleus and their blebs based on their
473 respective area. If the area of an object was below 100 μm^2 for confined conditions, it was considered
474 to be a bleb.

475 **DNA damage analysis** was automatically performed using the Find Maxima tool within each nucleus in
476 ImageJ/Fiji.

477 The percentage of **positive nuclear envelope area** corresponds to the excess area of the lamina envelope
478 compared to the nuclear area. This parameter was derived from methods used in [15,54]. The nuclear
479 envelope-positive area was assessed by thresholding the maximum intensity projection images of lamin
480 A/C staining obtained by confocal microscopy (x63 objective NA 1.25, Leica SP5) and merging them with
481 nuclei masks. This allowed us to study the laminas within the nucleus and provided information on the
482 proportion of area with laminas within the nucleus (positive area).
483 **Live movies** were analyzed manually by using either MTrackJ, or manual tracking and ROI manager tool
484 in ImageJ/Fiji plugin. Thus, we could measure nuclear areas over time in each phase of the cell cycle and
485 the corresponding duration of those phases.
486 For each experiment, at least three different areas within each confined zone of the confiner were
487 analyzed.

488 Statistics and reproducibility of experiments

489 Statistical data were expressed as mean ± standard deviation unless mentioned otherwise. Sample size
490 (n) and the number of repetitions (N) are specified in the text of the paper or figure legends. The
491 statistical significance between experimental conditions was determined using a two-tailed unpaired t-
492 test, Welch's test, Mann-Whitney test, or ANOVA after confirming that the data met appropriate
493 assumptions (normality distribution, homogeneous variance, and independent sampling). All data were
494 analyzed with GraphPad Prism 8.0. (San Diego, CA, USA). **** $P < 0.0001$, *** $P < 0.001$, ** $P < 0.01$, *
495 $P < 0.05$.

496 Supplementary Material 1 – Geometrical model

497 Confined nuclei can be modeled as a cylinder. Thus, their surfaces were calculated using the following
498 equations.

499 $$2\pi R_1 h + 2\pi {R_1}^2 = S_{app} \qquad \text{(Equation 1)}$$

500 With R_1, the diameter of the nucleus, h, its height, and S_{app}, its apparent surface.
501 R_1, the radius of this cylinder can then be extracted:

502 $$ {R_1}^2 + R_1 h - \frac{S_{app}}{2\pi} = 0 \qquad (2)$$

503 With a positive solution:

504 $$R_1 = \frac{-h+\sqrt{\Delta}}{2} \quad (4)$$

505 To compute the nuclear-envelope surface to add during division, we first calculated the surface of the
506 mother cell using equation 1 and then its volume. Using the obtained volume and equation 1 for two
507 cells, we finally computed the surface of the two daughter cells. For non-confined cells, we used a similar
508 approach with spheres rather than cylinders.

509 ## References

510 1. Butcher, D. T., Alliston, T. & Weaver, V. M. A tense situation: forcing tumour progression. *Nat. Rev.*
511 *Cancer* **9**, 108–22 (2009).
512 2. Helmlinger, G., Netti, P. A., Lichtenbeld, H. C., Melder, R. J. & Jain, R. K. Solid stress inhibits the growth
513 of multicellular tumor spheroids. *Nat. Biotechnol.* **15**, 778–783 (1997).
514 3. Jain, R. K., Martin, J. D. & Stylianopoulos, T. The role of mechanical forces in tumor growth and
515 therapy. *Annu. Rev. Biomed. Eng.* **16**, 321–46 (2014).
516 4. Mohammadi, H. & Sahai, E. Mechanisms and impact of altered tumour mechanics. *Nat. Cell Biol.* **20**,
517 766–774 (2018).
518 5. Sheridan, C. Pancreatic cancer provides testbed for first mechanotherapeutics. *Nat. Biotechnol.* **37**,
519 829–831 (2019).
520 6. Mpekris, F. *et al.* Combining microenvironment normalization strategies to improve cancer
521 immunotherapy. *Proc. Natl. Acad. Sci.* **117**, 3728–3737 (2020).
522 7. Friedl, P., Wolf, K. & Lammerding, J. Nuclear mechanics during cell migration. *Curr. Opin. Cell Biol.* **23**,
523 55–64 (2011).
524 8. Nader, G. P. de F. *et al.* Compromised nuclear envelope integrity drives TREX1-dependent DNA
525 damage and tumor cell invasion. *Cell* **184**, 5230-5246.e22 (2021).
526 9. Tse, H. T. K., Weaver, W. M. C. & Carlo, D. Increased asymmetric and multi-daughter cell division in
527 mechanically confined microenvironments. *PLoS ONE* **7**, 1–8 (2012).

528 10. Lancaster, O. M. *et al.* Mitotic Rounding Alters Cell Geometry to Ensure Efficient Bipolar Spindle
529 Formation. *Dev. Cell* **25**, 270–283 (2013).
530 11. Moriarty, R. A. & Stroka, K. M. Physical confinement alters sarcoma cell cycle progression and
531 division. *Cell Cycle* **17**, 2360–2373 (2018).
532 12. Gupta, V. K. & Chaudhuri, O. Mechanical regulation of cell-cycle progression and division. *Trends*
533 *Cell Biol.* **32**, 773–785 (2022).
534 13. Aureille, J. *et al.* Nuclear envelope deformation controls cell cycle progression in response to
535 mechanical force. *EMBO Rep.* **20**, 1–11 (2019).
536 14. Dantas, M., Oliveira, A., Aguiar, P., Maiato, H. & Ferreira, J. G. Nuclear tension controls mitotic
537 entry by regulating cyclin B1 nuclear translocation. *J. Cell Biol.* **221**, e202205051 (2022).
538 15. Lomakin, A. J. *et al.* The nucleus acts as a ruler tailoring cell responses to spatial constraints.
539 *Science* **370**, eaba2894 (2020).
540 16. Venturini, V. *et al.* The nucleus measures shape changes for cellular proprioception to control
541 dynamic cell behavior. *Science* **370**, eaba2644 (2020).
542 17. Raab, M. *et al.* ESCRT III repairs nuclear envelope ruptures during cell migration to limit DNA
543 damage and cell death. *Science* **352**, 359–362 (2016).
544 18. Xia, Y. *et al.* Rescue of DNA damage after constricted migration reveals a mechano-regulated
545 threshold for cell cycle. *J. Cell Biol.* **218**, 2542–2563 (2019).
546 19. Srivastava, N. *et al.* Nuclear fragility, blaming the blebs. *Curr. Opin. Cell Biol.* **70**, 100–108 (2021).
547 20. Prunet, A. *et al.* A new agarose-based microsystem to investigate cell response to prolonged
548 confinement. *Lab. Chip* **20**, 4016–4030 (2020).
549 21. Charras, G. T., Coughlin, M., Mitchison, T. J. & Mahadevan, L. Life and Times of a Cellular Bleb.
550 *Biophys. J.* **94**, 1836–1853 (2008).
551 22. MacIejowski, J. & Hatch, E. M. Nuclear Membrane Rupture and Its Consequences. *Annu. Rev. Cell*
552 *Dev. Biol.* **36**, 85–114 (2020).

553 23. Le Berre, M., Aubertin, J. & Piel, M. Fine control of nuclear confinement identifies a threshold
554 deformation leading to lamina rupture and induction of specific genes. *Integr. Biol. U. K.* **4**, 1406–1414
555 (2012).
556 24. Vargas, J. D., Hatch, E. M., Anderson, D. J. & Hetzer, M. W. Transient nuclear envelope rupturing
557 during interphase in human cancer cells. *Nucl. Austin Tex* **3**, 88–100 (2012).
558 25. Chow, K.-H., Factor, R. E. & Ullman, K. S. The nuclear envelope environment and its cancer
559 connections. *Nat. Rev. Cancer* **12**, 196–209 (2012).
560 26. Stylianopoulos, T., Munn, L. L. & Jain, R. K. Reengineering the Physical Microenvironment of
561 Tumors to Improve Drug Delivery and Efficacy: From Mathematical Modeling to Bench to Bedside.
562 *Trends Cancer* **4**, 292–319 (2018).
563 27. Pennacchio, F. A. *et al.* Force-biased nuclear import sets nuclear-cytoplasmic volumetric coupling
564 by osmosis. 2022.06.07.494975 Preprint at https://doi.org/10.1101/2022.06.07.494975 (2022).
565 28. Andreu, I. *et al.* Mechanical force application to the nucleus regulates nucleocytoplasmic
566 transport. *Nat. Cell Biol.* **24**, 896–905 (2022).
567 29. Elosegui-Artola, A. *et al.* Force Triggers YAP Nuclear Entry by Regulating Transport across Nuclear
568 Pores. *Cell* **171**, 1397-1410.e14 (2017).
569 30. Mistriotis, P. *et al.* Confinement hinders motility by inducing RhoA-mediated nuclear influx,
570 volume expansion, and blebbing. *J. Cell Biol.* **218**, 4093–4111 (2019).
571 31. Rosenblatt, J., Cramer, L. P., Baum, B. & McGee, K. M. Myosin II-Dependent Cortical Movement
572 Is Required for Centrosome Separation and Positioning during Mitotic Spindle Assembly. *Cell* **117**,
573 361–372 (2004).
574 32. Straight, A. F. *et al.* Dissecting Temporal and Spatial Control of Cytokinesis with a Myosin II
575 Inhibitor. *Science* **299**, 1743–1747 (2003).
576 33. Shah, P. *et al.* Nuclear Deformation Causes DNA Damage by Increasing Replication Stress. *Curr.*
577 *Biol.* **31**, 753-765.e6 (2021).

578 34. Pfeifer, C. R. *et al.* Constricted migration increases DNA damage and independently represses
579 cell cycle. *Mol. Biol. Cell* **29**, 1948–1962 (2018).
580 35. Shah, P., Wolf, K. & Lammerding, J. Bursting the Bubble – Nuclear Envelope Rupture as a Path to
581 Genomic Instability? *Trends Cell Biol.* **27**, 546–555 (2017).
582 36. Uhler, C. & Shivashankar, G. V. Regulation of genome organization and gene expression by
583 nuclear mechanotransduction. *Nat. Rev. Mol. Cell Biol.* **18**, 717–727 (2017).
584 37. Gonzalez-Suarez, I. *et al.* Novel roles for A-type lamins in telomere biology and the DNA damage
585 response pathway. *EMBO J.* **28**, 2414–2427 (2009).
586 38. Huang, R.-X. & Zhou, P.-K. DNA damage response signaling pathways and targets for
587 radiotherapy sensitization in cancer. *Signal Transduct. Target. Ther.* **5**, 1–27 (2020).
588 39. Mattout-Drubezki, A. & Gruenbaum, Y. Dynamic interactions of nuclear lamina proteins with
589 chromatin and transcriptional machinery. *Cell. Mol. Life Sci. CMLS* **60**, 2053–2063 (2003).
590 40. Patil, S. & Sengupta, K. Role of A- and B-type lamins in nuclear structure–function relationships.
591 *Biol. Cell* **113**, 295–310 (2021).
592 41. Rollin, R., Joanny, J.-F. & Sens, P. Cell size scaling laws: a unified theory. *BioRxiv 20220801502021*
593 1–20 (2022).
594 42. Jevtić, P. & Levy, D. L. Mechanisms of Nuclear Size Regulation in Model Systems and Cancer. in
595 *Cancer Biology and the Nuclear Envelope* (eds. Schirmer, E. C. & de las Heras, J. I.) vol. 773 537–569
596 (Springer New York, 2014).
597 43. de Las Heras, J. I. & Schirmer, E. C. The nuclear envelope and cancer: a diagnostic perspective
598 and historical overview. *Adv. Exp. Med. Biol.* **773**, 5–26 (2014).
599 44. Willis, N. D. *et al.* Lamin A/C is a risk biomarker in colorectal cancer. *PloS One* **3**, e2988 (2008).
600 45. Friedl, P., Wolf, K. & Lammerding, J. Nuclear mechanics during cell migration. *Curr. Opin. Cell*
601 *Biol.* **23**, 55–64 (2011).
602 46. Bell, E. S. *et al.* Low lamin A levels enhance confined cell migration and metastatic capacity in
603 breast cancer. *Oncogene* **41**, 4211–4230 (2022).

604 47. Zoetemelk, M., Rausch, M., Colin, D. J., Dormond, O. & Nowak-Sliwinska, P. Short-term 3D
605 culture systems of various complexity for treatment optimization of colorectal carcinoma. *Sci. Rep.* **9**,
606 7103 (2019).
607 48. Kuga, T. *et al.* Lamin B2 prevents chromosome instability by ensuring proper mitotic
608 chromosome segregation. *Oncogenesis* **3**, e94 (2014).
609 49. Yang, Z., Maciejowski, J. & de Lange, T. Nuclear Envelope Rupture Is Enhanced by Loss of p53 or
610 Rb. *Mol. Cancer Res.* **15**, 1579–1586 (2017).
611 50. Schirmer, E. C., Latonen, L. & Tollis, S. Nuclear size rectification: A potential new therapeutic
612 approach to reduce metastasis in cancer. *Front. Cell Dev. Biol.* **10**, 1022723 (2022).
613 51. Gorjánácz, M. Nuclear assembly as a target for anti-cancer therapies. *Nucl. Austin Tex* **5**, 47–55
614 (2014).
615 52. Rose, M., Burgess, J. T., O'Byrne, K., Richard, D. J. & Bolderson, E. The role of inner nuclear
616 membrane proteins in tumourigenesis and as potential targets for cancer therapy. *Cancer Metastasis*
617 *Rev.* **41**, 953–963 (2022).
618 53. Schmidt, U., Weigert, M., Broaddus, C. & Myers, G. Cell Detection with Star-Convex Polygons. in
619 *Medical Image Computing and Computer Assisted Intervention – MICCAI 2018* (eds. Frangi, A. F.,
620 Schnabel, J. A., Davatzikos, C., Alberola-López, C. & Fichtinger, G.) 265–273 (Springer International
621 Publishing, 2018). doi:10.1007/978-3-030-00934-2_30.
622 54. Purushothaman, D. *et al.* The transcription factor PREP1(PKNOX1) regulates nuclear stiffness,
623 the expression of LINC complex proteins and mechanotransduction. *Commun. Biol.* **5**, 1–14 (2022).

624

625

Acknowledgment

This work was supported by ANR Institut Convergence Plascan, the Institut Universitaire de France (IUF) and the ARC for part of M. Mouelhi salary. The authors would like to acknowledge C. Chaveroux, Marie Piecyk, C. Duret (CRCL) and S. Joly for the transfection and selection of HT-29-FUCCI cell line, R. Fulcrand for the preparation of 5-µm wafer molds, M. Mercury for the microscope holder and the press. G. Jardiné for his help to compute nuclear volume of control cells, B. Manship for English editing of the manuscript, as well as M. Piel for fruitful discussions of our results and careful reading of the manuscript.

Author contribution

S.M. and C.R. contributed equally to this work. S.M and C.R. supervised the project. M.M., S.M. and C.R. designed the research. M.M., A.S. performed the experiments. M.M., H.A. performed the modeling. M.M., A.S., S.M. and C.R. analyzed the data. M.M., S.M. and C.R. wrote the manuscript. All authors helped to edit the manuscript.

Supplementary figures

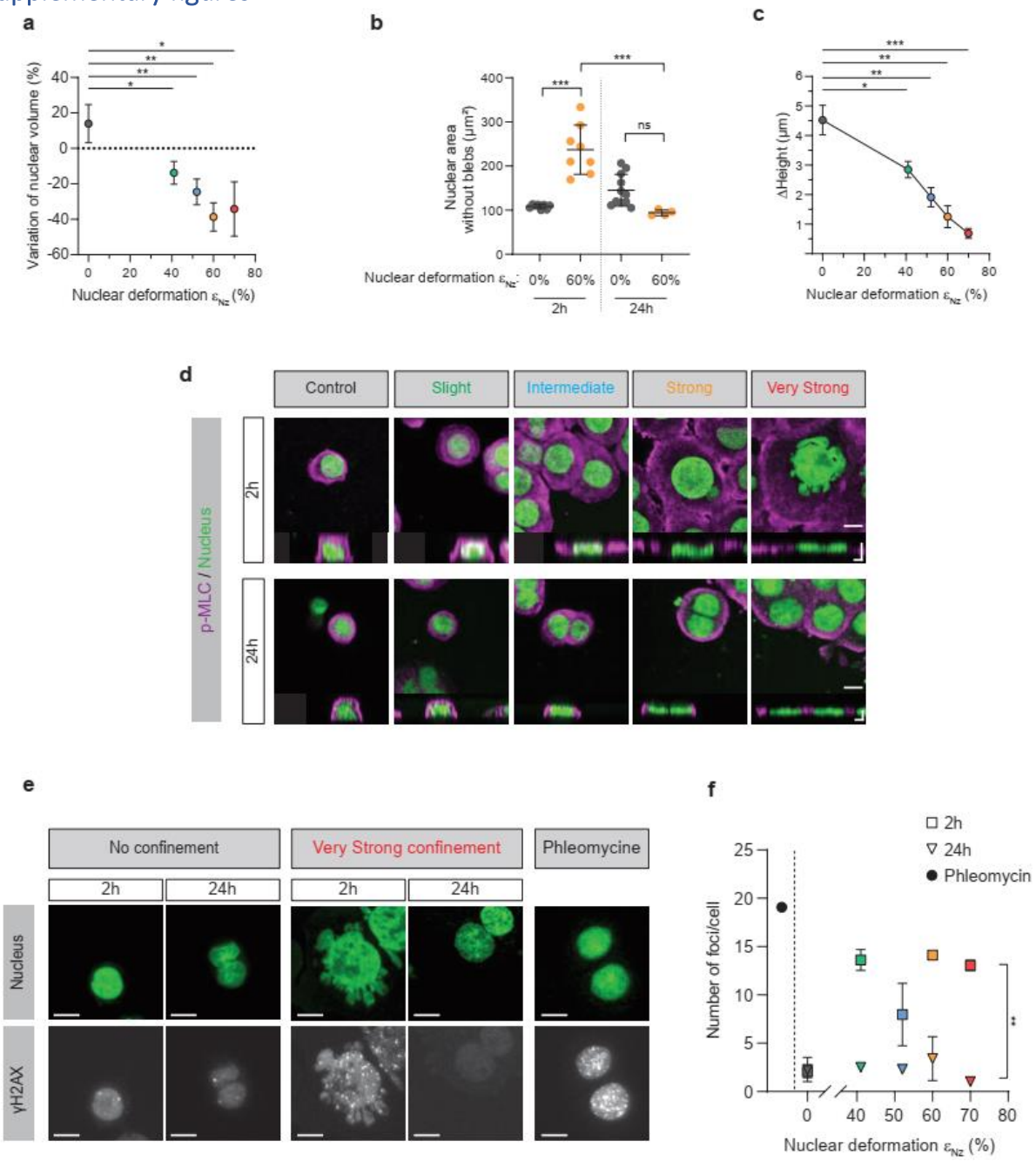

Figure 1 supp

(a) Variation of nuclear volume between 2 h and 24 h according to the nuclear deformation (which correspond to the height of the confinement). *N = 3 experiments with n > 5,000cells/experiment, unpaired t-test.* **(b)** Scatter plot of nuclear area without the blebs at 2 h and 24 h without confinement or under strong confinement. *N = 3 experiments with n = 31 cells, unpaired t-test.* **(c)** The difference in height between the nucleus and its cell membrane under increasing nuclear deformation. *N = 3 experiments with n > 5,000 cells/experiment*. **(d)** Representative images of stained nuclei and p-MLC in XY (scale bar = 10 µm) and its orthogonal view under increasing confinement (scale bar = 5 µm). **(e)** Representative images of nuclei and DNA damage, shown by stained γH2AX foci. Phleomycin is a drug that induces DNA damage used here as a positive control. *Scale bar = 10 µm*. **(f)** Quantification of the number of foci/cell, representative of the DNA damages according to an increase in nuclear deformation. *N = 2 experiments with n > 2000; mean ± SEM; unpaired t-test. Ordinary one-way ANOVA was also performed on all 24 h confinement conditions and was no significant*.

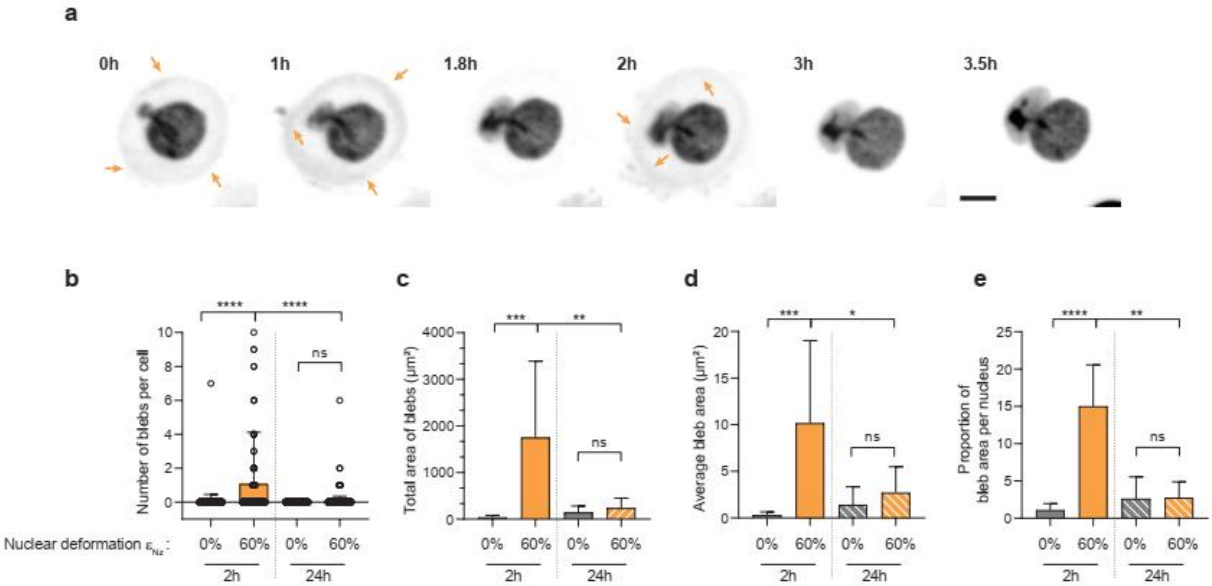

Figure 2 supp

(a) Sequential images of HT-29 cell expressing NLS-mKAte2 under strong confinement. Arrows show NLS-mKAte2 dye leakage within the cytoplasm indicating nuclear membrane rupture. *Scale bar = 10 µm.* **(b)** Bar chart of the number of blebs per cell according to the nuclear deformation (0% or 60%) at 2 h or 24 h of confinement. *N = 3 experiments with n = 1,376 cells, unpaired t-test.* **(c)** Quantification of the total area of blebs without confinement or under strong confinement (60% nuclear deformation) between 2 h and 24 h. *N = 3 experiments with n = 36, Mann-Whitney test.* **(d)** Quantification of the average area of blebs without confinement or under high confinement (60% nuclear deformation) between 2 h and 24 h. *N = 3 experiments with n = 36, Mann-Whitney test.* **(e)** Proportion (in percentage) of bleb area per nucleus without confinement or under high confinement (60% nuclear deformation) between 2 h and 24 h. *N = 3 experiments with n = 1,376 cells, Kolmogorov-Smirnov test.*

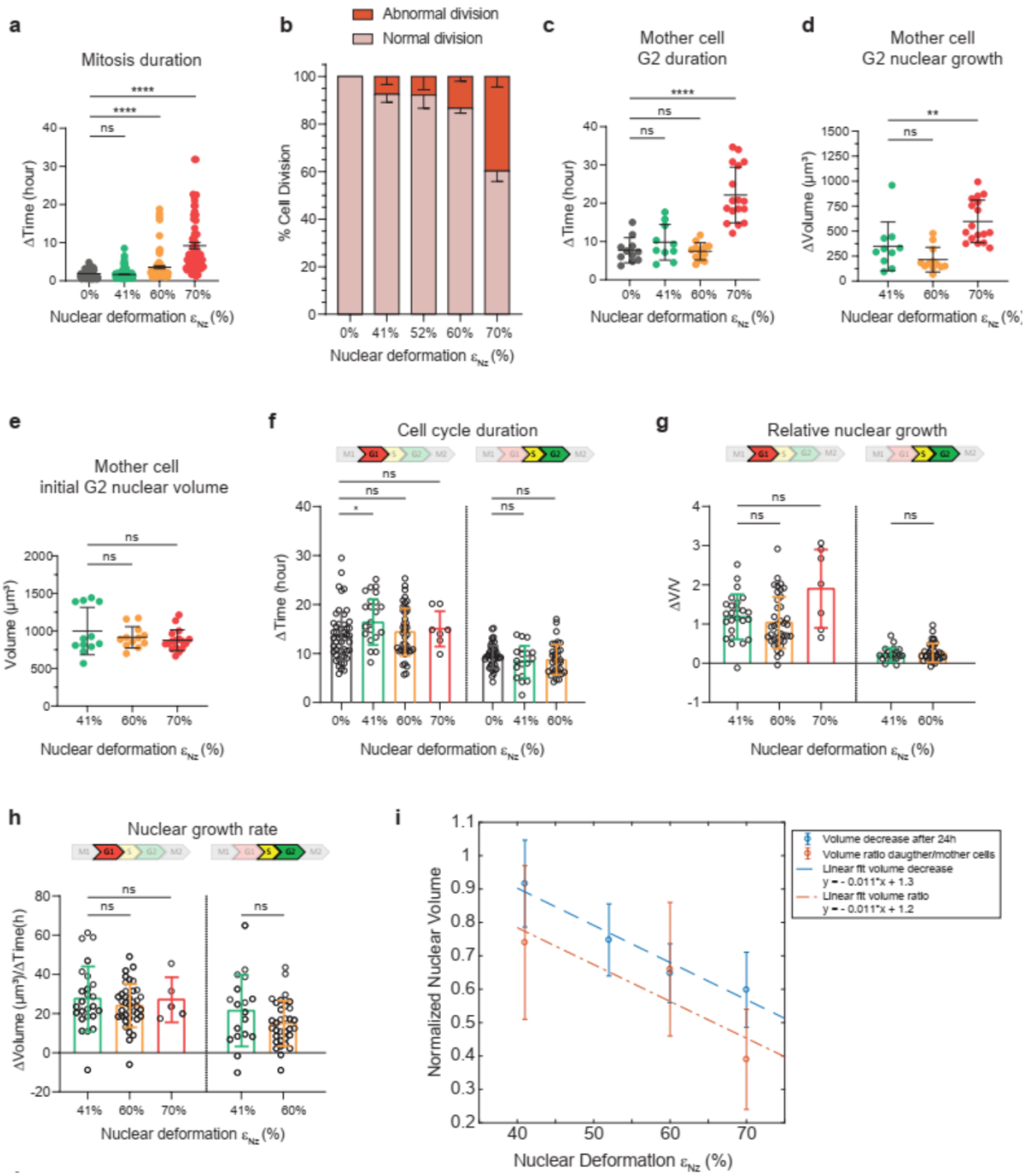

Figure 3 supp

(a) Scatter plot of mitosis duration under confinement. *N = 3 experiments with n = 398 cells; mean ± SEM, Mann-Whitney test.* **(b)** Percentage of normal or abnormal (multi-daughter cells and unevenly sized daughter cells) cell division under increasing confinement. *N = 2 experiments with n = 477 cells.* **(c)** Time of the mother cell spent in the G2-phase under confinement. *N = 2 experiments with n = 50 cells, unpaired t-test.* **(d)** Growth of mother cell nuclear volume in the G2-phase under different levels of confinement. *N = 2 experiments with n = 39 cells, Mann-Whitney test.* **(e)** Scatter plot of the initial nuclear volume of mother cells at the entrance of the G2 phase, *N = 2 experiments with n = 41 cells, unpaired t-test.* **(f, g, h)** Quantification of the duration **(f)**, the relative nuclear growth **(g)** and the nuclear growth rate **(h)** of HT-29 cell expressing Fucci under confinement during the G1-phase and the S-G2-phase after the first cell division. *N = 2 experiments with n > 200 cells, unpaired t-test for **(f, h)** and Mann-Whitney test for **(g)**.* **(i)** Normalized nuclear volume decrease at 24 h of confinement and nuclear volume decrease after mitosis as a function of nuclear deformation and their respective linear fit.

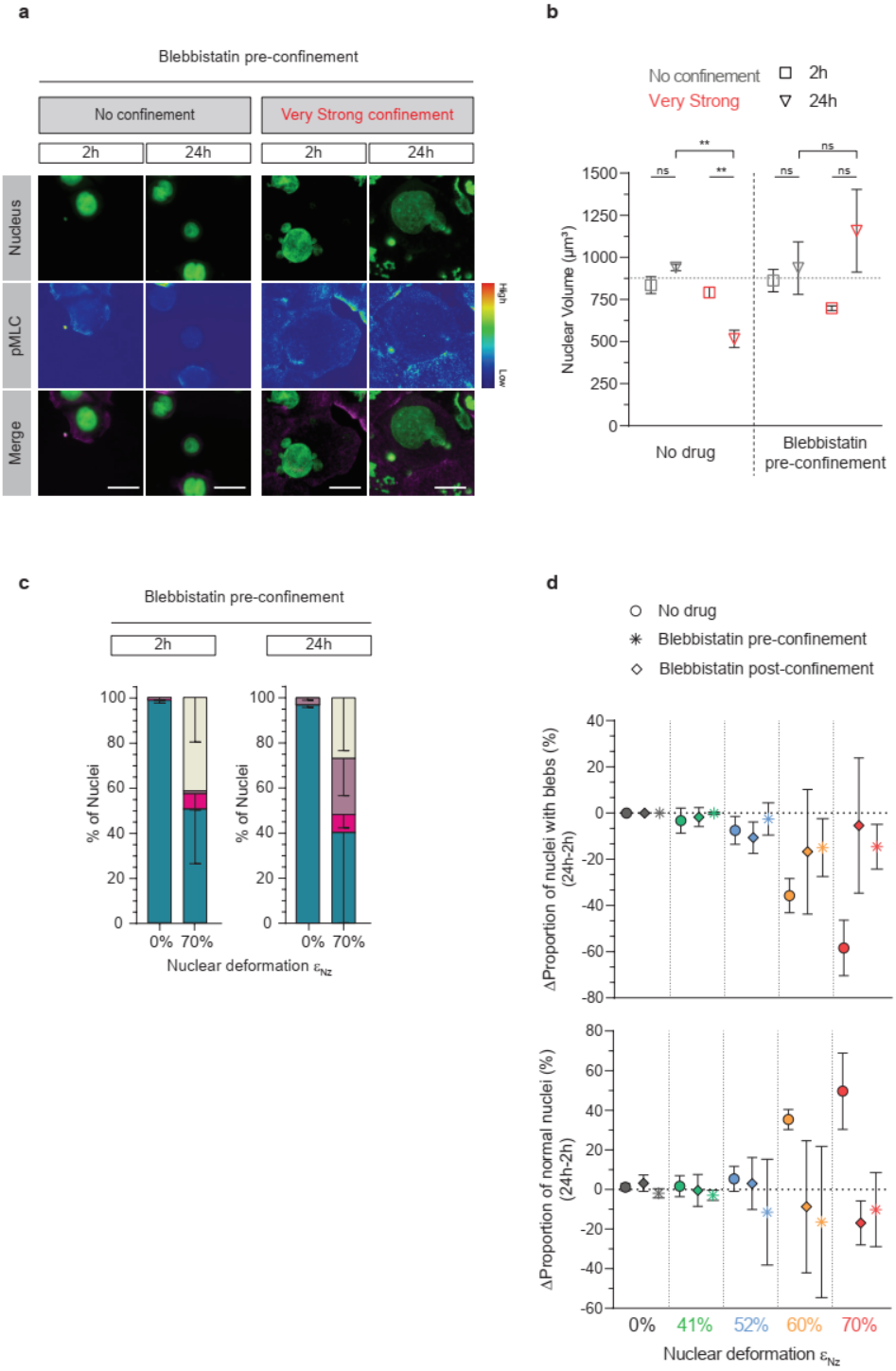

Figure 4 supp

(a) Representative images of stained nuclei and phospho-Myosin Light Chain (p-MLC) with Blebbistatin – added before confinement – at 2 h and 24 h without confinement or under very strong confinement. *Scale bar = 20 µm*. **(b)** Quantification of nuclear volume at 2 h and 24 h without drug or with Blebbistatin – added before confinement – without confinement or under very high confinement. *N = 3 experiments with n = 7,526 cells, mean ± SEM, unpaired t-test (for no drug conditions) or Mann-Whitney test (for Blebbistatin conditions).* **(c)** Quantification of nuclei with blebs, dividing, apoptotic or normal without confinement or under very strong confinement at 2 h and 24 h, with Blebbistatin – added before confinement –. *N = 3 experiments with n = 7,526 cells.* **(d)** Difference in proportion of normal nuclei and nuclei with blebs between 2 h and 24 h under several conditions: without drug, with Blebbistatin added pre-confinement and with Blebbistatin added post-confinement. *N = 3 experiments with n > 10,000 cells.*

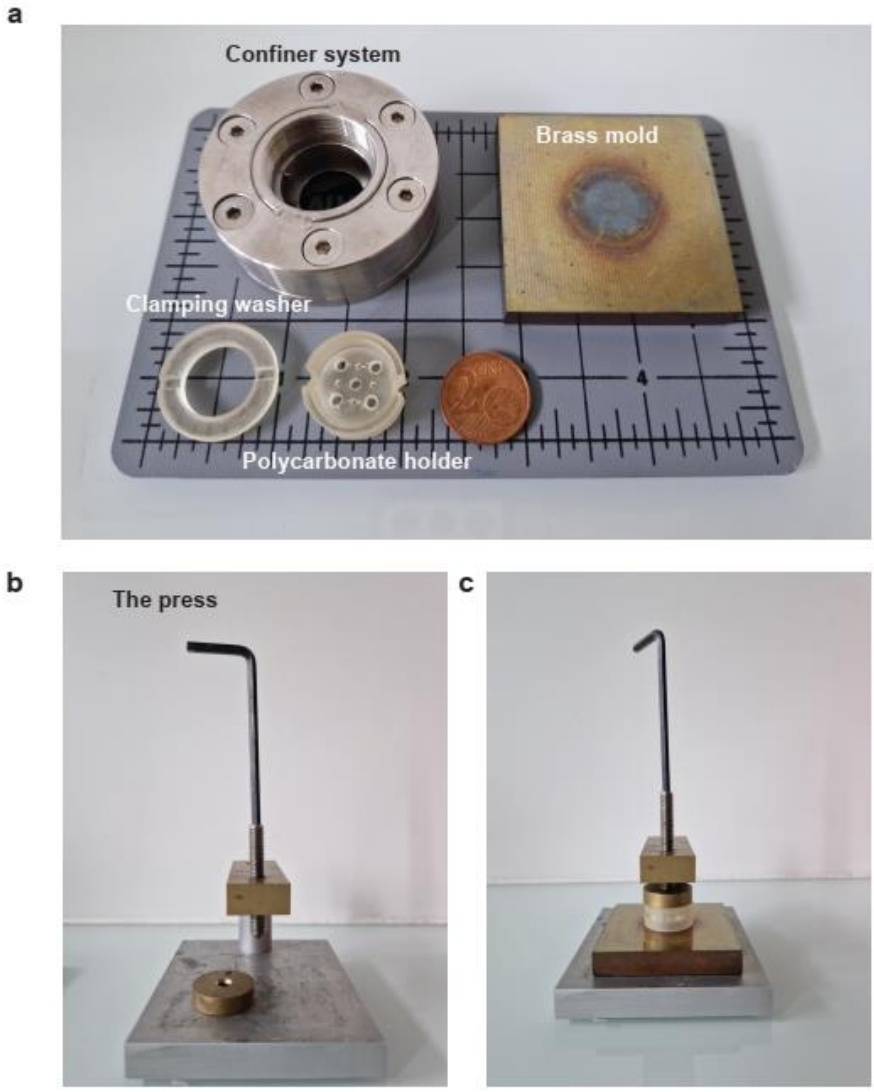

Figure 5 supp

(a) Picture of the principal components of the confiner system and their name next to the brass mold**. (b)** Picture of the press used to generate a uniform pressure during agarose molding. **(c)** Picture of the assembly process of agarose molding under press.

Movie 1 - Example of abnormal divisions under very strong confinement

Movie 2 - Example of blebs disappearance after mitosis.